USCAP

ARTICLE

Microvascularity detection and quantification in glioma: a novel deep-learning-based framework

Xieli Li[1,2] · Qisheng Tang[3] · Jinhua Yu[1,2,4] · Yuanyuan Wang[1,2,4] · Zhifeng Shi[3]

Abstract

Microvascularity is highly correlated with the grading and subtyping of gliomas, making this one of its most important histological features. Accurate quantitative analysis of microvessels is helpful for the development of a targeted therapy for antiangiogenesis. The deep-learning algorithm is by far the most effective segmentation and detection model and enables location and recognition of complex microvascular networks in large images obtained from hematoxylin and eosin (H&E) stained specimens. We proposed an automated deep-learning-based method to detect and quantify the microvascularity in glioma and applied it to comprehensive clinical analyses. A total of 350 glioma patients were enrolled in our study, for which digitalized imaging of H&E stained slides were reviewed, molecular diagnosis was performed and follow-up was investigated. The microvascular features were compared according to their histologic types, molecular types, and patients' prognosis. The results show that the proposed method can quantify microvascular characteristics automatically and effectively. Significant increases of microvascular density and microvascular area were observed in glioblastomas (95% $p < 0.001$ in density, 170% $p < 0.001$ in area) in comparison with other histologic types; increases were also observed in cases with TERT-mut only (68% $p < 0.001$ in density, 54% $p < 0.001$ in area) compared with other molecular types. Survival analysis showed that microvascular features can be used to cluster cases into two groups with different survival periods (hazard ratio [HR] 2.843, log-rank <0.001), which indicates the quantified microvascular features may potentially be alternative signatures for revealing patients' prognosis. This deep-learning-based method may be a useful tool in routine clinical practice for precise diagnosis and antiangiogenic treatment.

These authors contributed equally: Xieli Li, Qisheng Tang

✉ Yuanyuan Wang
yywang@fudan.edu.cn

✉ Zhifeng Shi
shizhifeng@fudan.edu.cn

1   Department of Electronic Engineering, Fudan University, 200433 Shanghai, China

2   Institute of Functional and Molecular Medical Imaging, Fudan University, 200040 Shanghai, China

3   Department of Neurosurgery, Huashan Hospital, Fudan University, 200040 Shanghai, China

4   Key Laboratory of Medical Imaging, Computing and Computer-Assisted Intervention, 200433 Shanghai, China

Introduction

Cerebral glioma is the most common malignant brain tumor in the central nervous system according to the Central Brain Tumor Registry of the United States (CBTRUS) [1]. In accordance with the latest World Health Organization (WHO) classification of brain tumors [2], well-established molecular parameters are incorporated into the diagnosis of diffuse gliomas. At present, the diagnosis of diffuse gliomas is not only based on histology but also on molecular diagnosis. For molecular diagnosis, isocitrate dehydrogenase (IDH) mutation status, codeletion of 1p and 19q, and mutations of the telomerase reverse transcriptase (TERT) promoter are three major biomarkers with significance [3, 4]. By using these three biomarkers, gliomas can be stratified into the following four molecular subtypes that contribute to accurate outcome prognostication: IDH-mut/1p/19q codeletion (i.e., triple positive, the subgroup of IDH-mut/1p/19q codeletion is expected to be triple positive because oligodendrogliomas are virtually always positive

for TERT promoter mutation.), IDH-mut only, TERT-mut only and triple negative. Among these subgroups, IDH-mut only, IDH-mut/1p/19q codeletion, and TERT-mut only are the most commonly seen, and they are highly correlated with histological astrocytoma, oligodendroglioma, and glioblastoma multiforme (GBM), respectively [5].

Microvascularization is of great significance in glioma development and malignant transformation, as well as being crucial for evaluating the effectiveness of antiangiogenic treatment. Since Brem et al. [6] proposed the idea of the neoplastic microvasculature quantification in histological specimens, microvascularity has been studied as a bio-marker for prognosis prediction and antiangiogenic drug responsiveness [7–9]. The histopathological diagnosis and grading of brain tumors have important implications in designing improved therapeutic strategies. Despite the development of advanced computer-aided tools, the eva-luation of histological specimens performed by pathologists is still the gold standard for the typing and grading of brain tumors. This process is time-consuming with inter- and intra-observer variability that cannot be ignored. Inter-observer variability and erroneous perception of tumor histology can result in a patient being over- or undertreated [10]. Therefore, accurate quantitative evaluation of micro-vasculature is required in the histological analysis of glioma.

Currently, machine-learning methods, particularly deep-learning algorithms, have been widely used in digital his-tological image analysis and have reached the diagnostic accuracy of humans [11–13]. In 2016, an automated fra-mework that combines the convolutional neural network (CNN) with the deformable model was proposed for nucleus segmentation of brain tumor, pancreatic neu-roendocrine tumor, and breast cancer. This model was found to outperform conventional segmentation methods [14]. A spatially constrained CNN and a softmax CNN were utilized in detection and classification of nuclei in routine colon cancer [15]. Subsequently, CNNs with more com-plicated architecture were proposed for automating the grading of gliomas [16]. For breast cancers, deep neural networks were applied in mitosis detection [17] and Goo-gLeNet was used for detection of cancer metastases [18]. With the development of network research, fully convolu-tional networks (FCN) have predominated semantic seg-mentation. U-net was proposed for the segmentation of neuronal structures in electron microscopic stacks [19]. However, rarely have automated methods been proposed for the detection and segmentation of microvessels in hema-toxylin and eosin (H&E) stained histological specimens. Nearly all of the computer-assisted microvasculature ana-lyses are based on morphometry by manual segmentation or simple thresholding of immunohistochemical staining ima-ges using hot-spot selection strategy [20–22].

In this study, we established an automated computer-assisted, deep-learning-based approach to thoroughly and accurately detect and segment microvessels and objectively quantify the histological microvascular pattern (MVP) configuration in whole H&E-stained specimens. As micro-vascularity has been shown as an alternative feature for differentiating gliomas of different subgroups, we intended to explore the effectiveness of the proposed approach in clinical practice by applying it in the microvascularity analysis of various glioma subtypes. Histological subtypes, genotypes, and prognosis were included in the correlation analysis with microvascularity. The workflow of the pro-posed approach is presented in Fig. 1.

Materials and methods

Case selection

This study enrolled 350 adult patients who were pathologi-cally diagnosed with glioma between 2012 and 2017 at the Huashan Hospital of Fudan University. The cases were divided into two groups. Some of the cases (58 cases) were used for network training and the others (292 cases) were used for statistical analysis (Table 1). The tumor spe-cimens, which were made into H&E-stained slides, were reviewed and confirmed according to the current WHO 2016 criteria. All of the analyzed samples were from pretreatment surgeries. These slides were scanned by Aperio ScanScope XT and saved as whole-slide images (WSIs). The size of WSIs in the overall dataset varies between $15{,}755 \times 23{,}570$ and $71{,}047 \times 123{,}746$ pixels, with an average value of $63{,}224 \times 74{,}240$. In addition, the results of the molecular diagnosis for all cases were retrieved from the Huashan Molecular Database. Genotyping of all the cases were per-formed according to the system as previous reported: IDH mutation only, IDH-mut/1p/19q codeletion, TERT mutation only, and triple negative. We evenly selected the training cases according to their histological types and molecular types for the sake of diversity. Five hundred and eighty patches were extracted from the 58 WSIs and each case provided ten patches with different microvessels. For nega-tive samples, 62 patches without microvessels were collected from the blank background, normal cortex, hemorrhage area, and the tumor area. Some of the negative samples are similar to the positive samples. The size of the smallest patch is 204×220 pixels, the largest patch is 4594×3718 and the average is 763×815 pixels. We quadrupled these patches with random rotation and color disruption and the final number of the training samples was 2568 patches. For the test image, we collected one patch with microvessels, in part or in whole, from each WSI in the dataset for statistical analysis which is independent of training cases and also extract 36
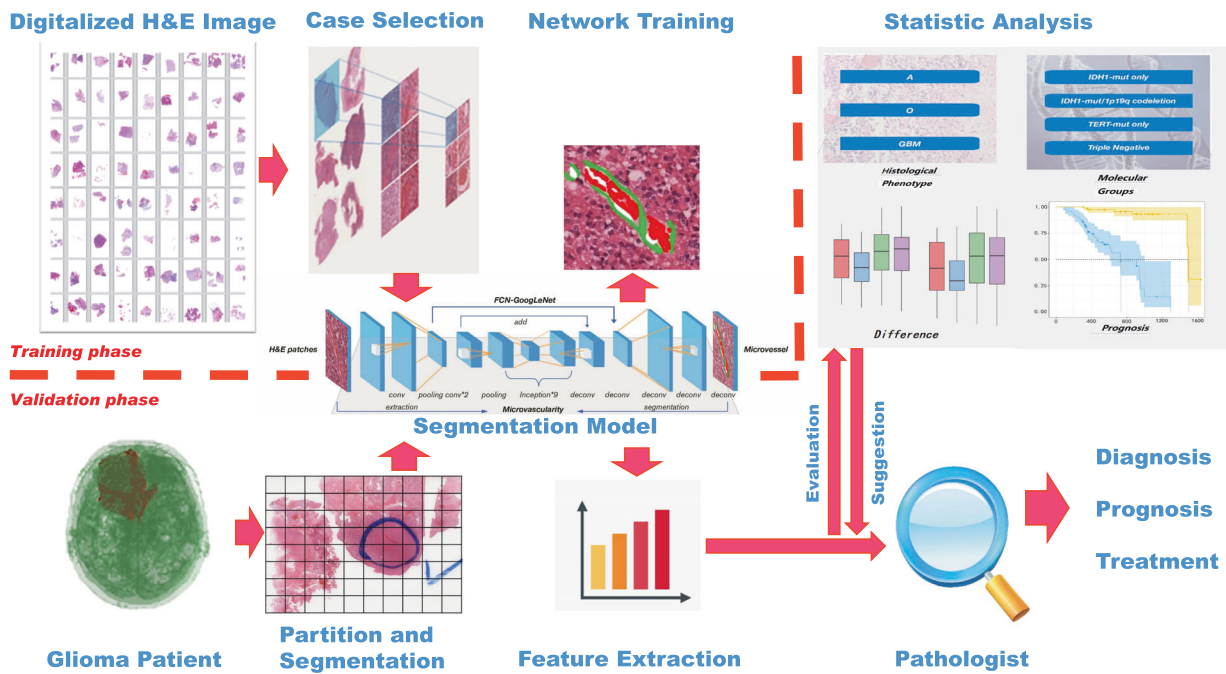
Fig. 1 The workflow of microvascular assessment. The top left part of the figure is a schematic diagram of the training phase. Images with annotations are selected from WSIs for segmentation model training. The rest of the figure is a schematic diagram of the clinical validation phase. Microvascular patterns in patient's WSI are assessed by our method and suggestions about diagnosis, prognosis and anti-angiogenesis treatment are provided for pathologists

Table 1 Patients' characteristics

	Network training set, N (%)	Statistics analyzing set, N (%)	TCGA test set[a], N (%)
No. of patients (WSIs)	58	292	35
Age	50.8 ± 14.5	47.2 ± 15.3	48.8 ± 14.6
Gender			
Women	22 (37.9)	139 (47.6)	14 (40.0)
Men	36 (62.1)	153 (52.4)	21 (60.0)
Histology type			
Astrocytoma	20 (34.5)	137 (46.9)	10 (28.6)
Oligodendroglioma	17 (29.3)	66 (22.6)	10 (28.6)
Glioblastoma	21 (36.2)	89 (30.5)	15 (42.8)
Molecular type			
IDH-mut only	10 (17.2)	82 (28.1)	–
IDH-mut/1p19q codeletion	10 (17.2)	80 (27.4)	–
TERT-mut only	10 (17.2)	77 (26.4)	–
Triple negative	10 (17.2)	53 (18.1)	–
Other	18 (31.2)	0 (0.0)	–
Follow-up investigated	0 (0.0)	179 (61.3)	–

[a]WSIs downloaded from TCGA database are for the segmentation test, therefore the molecular and prognostic information are not collected

negative patches. In this way, we obtained a test dataset of 328 images, which could ensure the quality of the segmentation results in the following step Moreover, we downloaded 35 WSIs from TCGA GBM and LGG database and extracted 195 images including 30 negative samples as the second independent test set for validation of robustness. The details are shown in Table 2. Follow-up information was available for 179 patients.

Methodology for segmentation and feature extraction

Fully convolutional network for microvessel segmentation

In the microvessel segmentation task, methods that can produce semantic segmentation results that are end-to-end and ultimately pixel-to-pixel are required. FCNs are alternative approaches for this task [23]. FCN consists of convolutional layers, pooling layers, activating layers, and deconvolutional layers. By replacing fully connective operations with convolutional operations, CNNs are able to predict classifications of several local parts of the input images rather than one global classification result for each image. Through deconvolutional operations, the local classification results will produce coarse output maps that share the size of the input images. To our knowledge, among the layers of CNNs, feature maps from shallower layers maintain lower level visual features, but more spatial location features and vice versa. Combining features from shallower layers with coarse deconvolutional results makes the output

Table 2 Dataset for microvessel segmentation

		Subtype	Training set	Testing set	TCGA
WSI	Histology	Astrocytoma	20	137	10
		Oligodendroglioma	17	66	10
		Glioblastoma	21	89	15
		Total	58	292	35
	Molecular	IDH-mut only	10	82	–
		IDH-mut/1p19q codeletion	10	80	–
		TERT-mut only	10	77	–
		Triple negative	18	53	–
		Total	58	292	–
Patch	Positive sample		2320	292	165
	Negative sample		248	36	30
	Total		2568	328	195
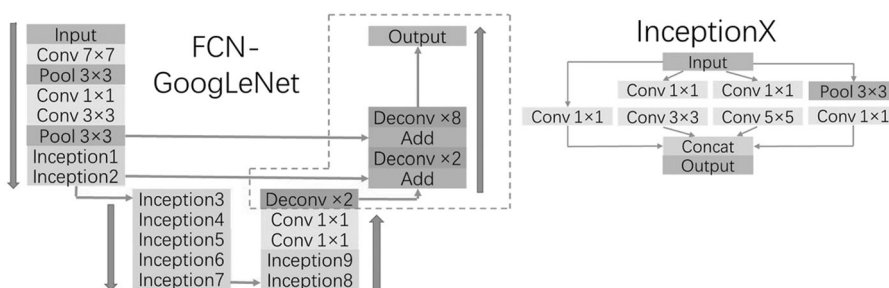
Fig. 2 The detailed architecture of the FCN-GoogLeNet. The FCN-GoogLeNet consists of nineteen layers, including five convolutional layers, two max pooling layers, nine Inception modules, and three deconvolutional layers. Each Inception module has multiscale convolution filters with different depth, which enable the network to identify targets of different sizes

maps more precise and detailed. Compared to conventional classification models with a slide window, FCNs split more finely and cost less time. In this study, we tested various kinds of networks with fully convolutional structures including FCN-GoogLeNet [23, 24], FCN-VGG16 [23, 25], and U-Net [19] (see detailed structure in Fig. S1).

Before the process of training, we collected manually labeled images and augmented these patches by rotating, flipping, and adding color imbalance to establish the training set. Experienced physicians from Huashan Hospital were invited to label the dataset. Two pathologists segmented the images independently and checked each other's results. The ground truth was determined by averaging two results unless there was a disagreement between two pathologists. In such cases, a third expert judged the results and determined the final label. The segmentation images consist of four categories: microvessel, red blood cell (RBC), tissue stroma, and blank background. Each of the above networks was trained by the stochastic gradient descent algorithm with learning rate dropping gradually until the loss functions of both training set and validation set no longer declined. We set the training upper limit to 200 epochs because all models reach convergence. After the training, these networks were modified to produce microvascular regions.

Three different kinds of FCNs with their deformations were applied in the segmentation task and we used a series of independent annotated images to validate the performance of these models. The pixel accuracy (PA) of the image, mean pixel accuracy (MPA) of the four classes, the mean intersection over union (MIU), the frequency weighted IU (FWIU), and the dice coefficient (DICE) of the microvessel regions were the five critical properties that were evaluated.

For optimal reasons, we chose the FCN-GoogLeNet as the final segmentation model in further experiments (see Fig. 2).

Recognition of microvessels

We adopted some conventional image processing methods to refine the segmentation results. First, to maintain the segmentation integrity, small holes in the microvascular regions were filled and tiny microvascular patches outside the main part of the vascular regions were removed. Second, due to the segmentation results that indicated that one vessel could be separated into segments, these connected regions were merged into several microvessels according to relative size, location, and distance. Regions that share a similar

direction and are located close to each other are more likely to be recognized as one vessel. Moreover, small regions surrounding a big vessel are more likely to be regarded as extensions of the vessel. Third, structural information was taken into consideration during recognition. An annular structure formed by microvascular regions with a blank hole or RBC in the center is likely a single microvessel and so are the structures consisting of linear arranged vascular regions. Finally, the automatic threshold segmentation method was applied in the potential microvascular region to find endothelial cells, because the state of each microvessel depends on these cells. Microvessels with a thick layer of endothelial cells are considered to exhibit vascular endothelial cell proliferation, i.e., abnormal vessels.

Feature extraction

Clinically, characteristics such as MVP, microvascular area (MVA), and microvessel density (MVD) are calculated to reflect the microvascular state of the glioma [20, 21, 26]. In this study, we utilized these quantitative indices and added some new features to present the microvascular characteristics. The features involved in our study are listed in Table 3 and the details are provided in Table S1.

Microvascularity analysis

A correlation analysis was performed on all microvascularities to study the consistency and independence between some features. Then, three distinct scenarios were involved in the study:

(1) The glioma cases were divided into three histology subtypes: astrocytoma, oligodendroglioma and glioblastoma, and the quantitative microvascular

Table 3 Microvascular features

Feature category	Feature name	Feature number
Density	(1) Microvascular density	1
Area	(2) Microvascular area	1
Size	(3) Area of single microvessel	8
	(4) Length of single microvessel	
Shape	(5) Eccentricity of microvessel	4
Cluster degree	(6) Distance from center	4
Order degree	(7) Direction entropy	2
Supply area	(8) Area of microvascular blood supply	1
Hyperplasia degree	(9) Ratio of endotheliocytes	4
	(10) Ratio of proliferating microvessels	

differences were compared.

(2) The correlation between genotypes and microvascular property were explored by comparing four molecular types: IDH-mut only, IDH-mut/1p/19q codeletion, TERT-mut only and triple negative. This analysis was repeated in all cases and in low grade cases.

(3) We proposed a framework for microvascularity assessment in which cases were grouped by clustering some specific microvascular features. Survival analysis revealed a close relationship between multiple quantitative features and the survival time of patients, which indicates that microvascularity could distinguish patients with different prognoses as an alternative indicator.

Statistic processing

For correlation analysis, the data were neither normalized nor adjusted for the sake of assessing the accuracy of the extracted features. A correlation coefficient matrix was used to visualize the associations.

For the variation analysis, the Bartlett test was used to assess the homogeneity of variance of the features among the different types. The differences among groups were tested for significance by analysis of variance and the significance of difference between each two groups was tested by the student's t test (T test) if the data satisfied the homogeneity of variance (på 0.05). Otherwise, ($p \leq 0.05$), the Kruskal–Wallis (KW) test was utilized to test the significant differences between groups and the significance of difference between each two groups was evaluated by the Wilcoxon rank sum test.

In survival analysis, first we separated the 179 cases by 500 days of survival because many studies show that the median survival time of GBM is 15–17 months [2]. Since GBM has the worst prognosis, astrocytomas or oligodendrogliomas that tend to be GBM in OS also have a bad prognosis. Then we calculated the normalized clustering centers of the two groups (OS < 500 days and OS ≥ 500 days). The cut-off values were the mean values of the two clustering centers. Next, the cohort was regrouped into high-risk group and low-risk group according to the cut-off values, with each feature determining a grouping situation. Finally, we did survival analyses on these grouping situations.

Overall workflow

As shown in Fig. 1, our workflow consists of model training, feature extraction, statistical analysis, and validation. For patient level assessment, the WSI was cropped into non-overlapping patches of 1792 × 1792. Before segmentation,

Fig. 3 Segmentation results of five FCN model. Six typical images are arranged in rows with the first three rows from our independent testing set and the last three rows from TCGA database. Columns from left to right are the original image, the segmentation ground truth, the result of FCN-GoogLeNet, the result of FCN-VGG with 8 times upsampling, the result of FCN-VGG with directly 32 times upsampling, the result of U-Net with 4 downsampling layers and the result of U-Net with 5 downsampling layers
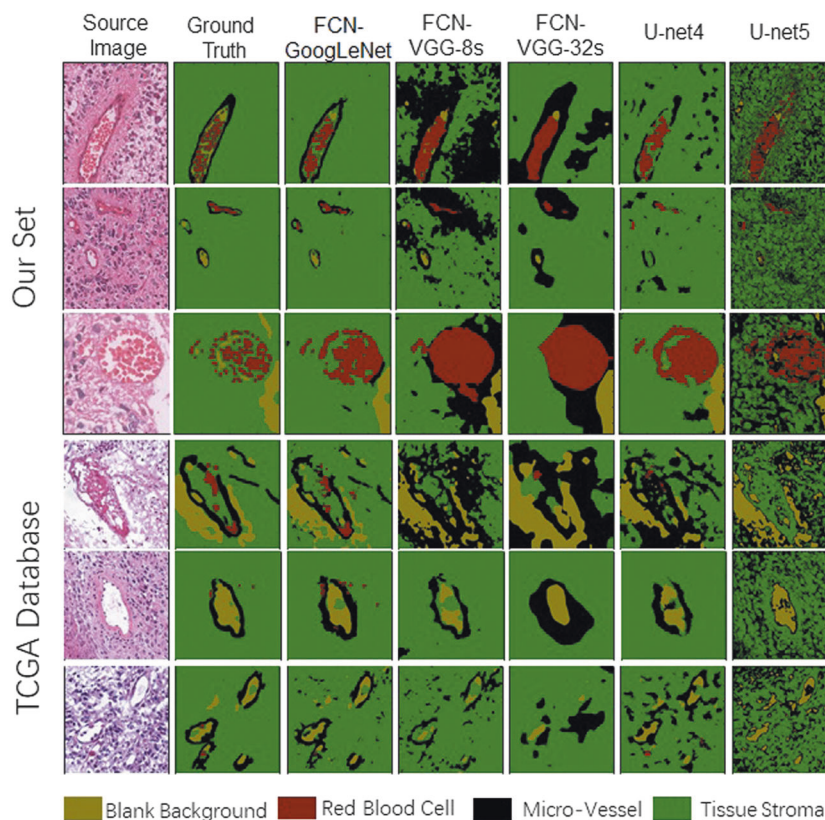
patches were filtered through a threshold value to ensure the validity of the contents. After segmentation and postprocessing, microvascularity was quantified, synthesized, and analyzed. The assessment about the degree of angiogenesis, the risk group belonging and the other details are designed to help pathologists to make a diagnosis, predict prognosis, and design treatment.

Experimental environment

A Dell Precision Tower 7910 workstation with an Intel(R) Xeon(R) CPU E5-2687W v4 @3.00 GHz processor, 64.0 GB RAM and NVIDIA TITAN Xp GPU is involved in our experiment. The programming tool was MATLAB R2017a with the MatCovNet toolkit. The statistical analysis was processed by R version 3.4.2.

Results

Segmentation and recognition

A total of 328 testing images in our dataset with manually segmented results were used in the evaluation of the microvessel segmentation. Before segmentation, these images were enlarged to the nearest multiple of 32 and so

were the corresponding annotations because they need to be down sampled five times in FCN models. The segmentation results and quantitative assessment indicators of the above five FCN models were compared and are listed in Fig. 3 and Table 4. Both visual feeling and quantitative indicators show that the FCN with a GoogLeNet structure outperformed the others. TCGA test data showed that there was a slight decrease in all five methods' performances. Considering the source of the two test sets and the segmentation performance, the FCN with a GoogLeNet structure is robust enough in the further experiment and the decrease is acceptable. Thus, we then used this FCN network as the segmentation model.

The postprocessing approaches described in the Methods section were conducted for microvessel recognition. We compared the microvascular number of the algorithm with the ground truth of the 328 testing images. The results of postprocessing and microvessel counting are shown in Fig. 4 and Table 5. Our method was able to correctly count the number of microvessels in most of the images. However, the absolute error increases as the image complexity increases. In the WSI level segmentation and recognition, the scanning window was set to 1792×1792. Microvessels are spaced sparsely among most of the WSI and the appropriate segmentation window limits the image complexity, thus the method precisely identified the vascularity.

Table 4 Segmentation performance of five FCN models on two independent testing sets

Network	PA		MPA		MIU		FWIU		DICE	
	Ours	TCGA	Ours	TCGA	Ours	TCGA	Ours	TCGA	Ours	TCGA
FCN-GoogLeNet	0.957	0.892	0.549	0.554	0.486	0.476	0.814	0.798	0.954	0.905
FCN-VGG-8s	0.853	0.801	0.540	0.505	0.374	0.390	0.689	0.729	0.830	0.843
FCN-VGG-32s	0.896	0.775	0.439	0.452	0.337	0.336	0.651	0.681	0.859	0.837
U-net4	0.849	0.801	0.465	0.440	0.352	0.348	0.667	0.732	0.826	0.845
U-net5	0.603	0.574	0.390	0.331	0.261	0.262	0.563	0.520	0.583	0.578

Fig. 4 Recognition results of the proposed method. Six typical images are arranged in column. Rows from top to bottom are the original image, the initial result of FCN-GoogLeNet, the recognition result of microvessel, the detected endothelia cells, the true number of microvessels and the prediction number of microvessels
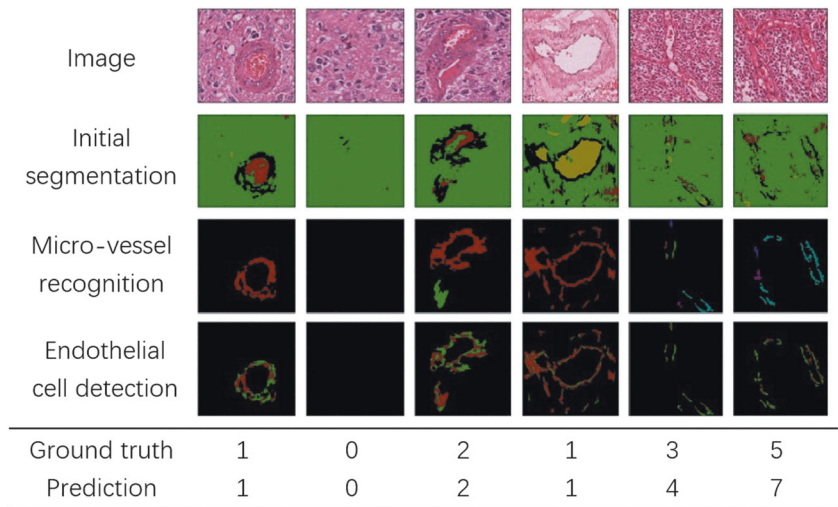
Ground truth	1	0	2	1	3	5
Prediction	1	0	2	1	4	7

Table 5 Performance of microvessel counting

Criteria	Value
Ground truth (mean ± sd)	0.87879 ± 1.03741
Prediction (mean ± sd)	0.90909 ± 0.93302
Absolute error (mean ± sd)	0.33333 ± 0.63564
Relative error (mean ± sd)	0.18687 ± 0.41995
Accuracy (%)	75.8
Ratio of absolute error ≤ 1 (%)	90.9

At the WSI level, a positive sample is defined as the area of microvessel while the negative sample is defined as the area of the other three categories. The false positive rate is 5.06% and the false negative rate is 22.40% at WSI level. Even though the false negative rate is slightly high, as long as the majority of the microvessel is identified, morphological features are valid and the model works well in the workflow.

Correlations between microvascular features

A correlation matrix (Fig. 5) shows the relationships between various microvascular features. The density, the cluster degree, the area, the number of nuclei, the size, and the length of the microvessels are highly correlated with each other ($r = 0.31$–0.99). This indicates that cases with a higher degree of angiogenesis are not only richer in the number of microvessels but also bigger in size. The area of nuclei is related to the proportion of proliferating vessels ($r = 0.93$), indicating that the phenomenon of angiogenesis is accompanied by endothelial cell proliferation. Moreover, a relationship ($r = 0.3$) exists between the shape and supply area, which means that a long strip of blood vessels can supply a larger area of tissue than a cluster of blood vessels. The strong negative correlation coefficient between order and supply area is caused by the direction of entropy. A low value of entropy relates to the regular arrangement of vessels and large supply area. These findings partly validate the effectiveness of our model in microvascular assessment.

Validation of distinct histopathology subtypes

Histopathology subtyping information of the glioma is utilized to validate the effectiveness of the extracted vascularity. The microvascular features of three pathological subtypes, astrocytoma, oligodendroglioma, and glioblastoma, were compared and are shown in Figs. 6, S2 and Table S2. Significant differences appeared in the comparison of vascular density, area, length, shape, distance, and other properties. Our findings are highly consistent with the pathological fact that glioblastoma is the most malignant

glioma with microvascular proliferation [2]. It is clear to see that the level of most properties in glioblastoma, particularly MVD and %MVA, is higher than in astrocytoma (95% and 170% higher, respectively) and oligodendroglioma (81% and 113% higher, respectively). In the category of lower grade gliomas, the vascular property of astrocytoma can be hard to distinguish from oligodendroglioma, except for the larger size of microvessels (11% larger) and greater number of endothelial cells (13% more) in oligodendroglioma.
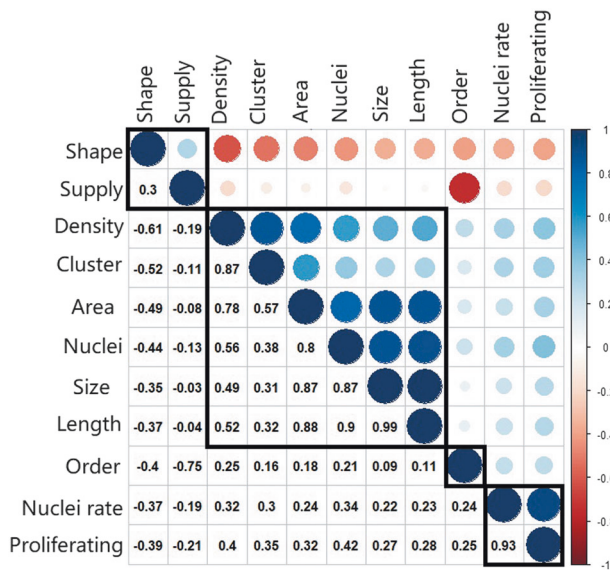

Fig. 5 Correlation matrix of the representative microvascular features. Shape: average eccentricity of microvessels (E_{avg}); Supply: average area of microvascular blood supply (*Sup*); Density: microvascular density (*MVD*); Cluster: average cluster degree (D_{avg}^{-1}); Area: percentage of microvascular area (*%MVA*); Nuclei: average number of nuclei in one vessel (N_e); Size: average area of one vessel (A_{avg}); Length: average length of one vessel (L_{avg}); Order: entropy of the vascular orientation (Ent^1); Nuclei rate: area ratio of endothelia cells to vessels (R_e); Proliferating: proportion of proliferating vessels (R_p). The upper part uses color to visualize the relationship and the lower part shows the coefficient. Features with high correlations are clustered into one black rectangle
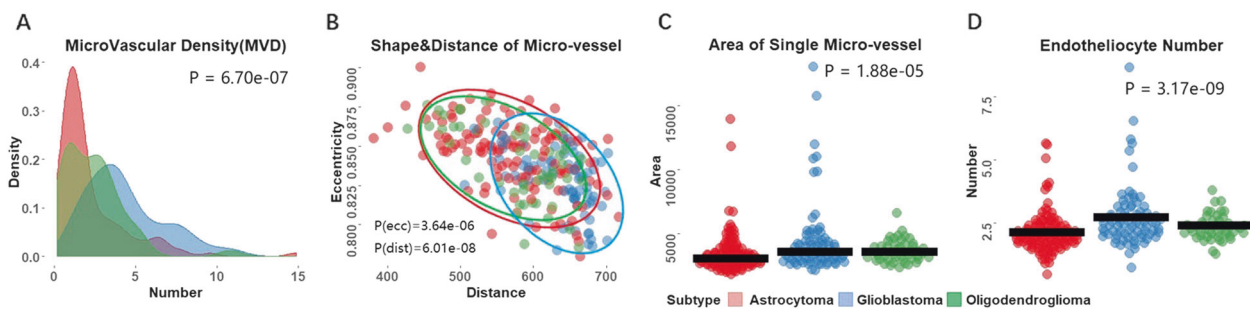
The outliers in Fig. 6 are shown to be GBM cases with hyperactive angiogenesis and astrocytoma cases with interfering extraneous normal tissues. These results indicate that our method can precisely extract the features of microvessels.

Validation of distinct genotypes

In regard to genotype correlation, we observed that part of the microvascular properties was significantly different among the cases. TERT-mut only and triple negative types have more diffuse microvessels (D), more microvascularity and a larger area (MVD and %MVA) than the other two types (~9%, 68%, and 54%, respectively), and the high levels are significant ($p < 0.05$), which shows their malignancies. In contrast, the blood supply area (Sup) is significantly higher in IDH-mut only and IDH-mut/1p/19q codeletion than the other two (38%). In addition, only TERT-mut only is significantly different from the other three in terms of E, Ent, R, and N. A lower value of E means that the vessels are closer to a circle or ring shape; higher Ent correlates to a more chaotic vascular arrangement, and a higher R and N refer to the higher proliferating degree of TERT-mut only. Moreover, the triple negative type has the smallest size of vessel (A, L), which means angiogenesis is common in this genotype. The results are shown in Figs. 7, S3, and Table S3. The outliers in Fig. 7 are the same cases seen in Fig. 6.

Even in lower grade gliomas, there are significantly more microvessels in the TERT-mut only and triple negative types than the other types (51% higher in %MVA, 64% higher in MVD). Although TERT-mut only has the most abundant endothelial cells and triple negative has the smallest area, the four genotypes are nearly the same in terms of proliferation degree and the size of vessels, which is an unusual phenomenon in lower grade gliomas. The differences of genotype are shown in Figs. 8, S4, and Table S4.

Fig. 6 Comparison of the vascularity between pathological subtypes. **a** The probability distribution map of microvascular density. **b** The scatter diagram of the average eccentricity and the average distance from cluster center of microvessels (the principal components of each subgroup are circled by an ellipse of the corresponding color). **c** The jitter graph of the average area of microvessel (the mean value is given by the black line). **d** The jitter graph of the average number of endothelial cell per microvessel (the mean value is given by the black line). *P* values obtained by significance analysis are given in the graph
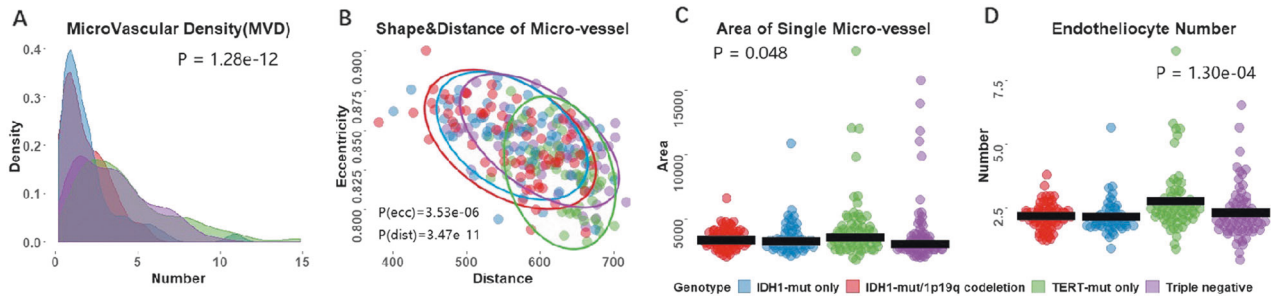
Fig. 7 Comparison of the vascularity between genotypes. **a** The probability distribution map of microvascular density. **b** The scatter diagram of the average eccentricity and the average distance from cluster center of microvessels (the principal components of each subgroup are circled by an ellipse of the corresponding color). **c** The jitter graph of the average area of microvessel (the mean value is given by the black line). **d** The jitter graph of the average number of endothelial cell per microvessel (the mean value is given by the black line). *P* values obtained by significance analysis are given in the graph
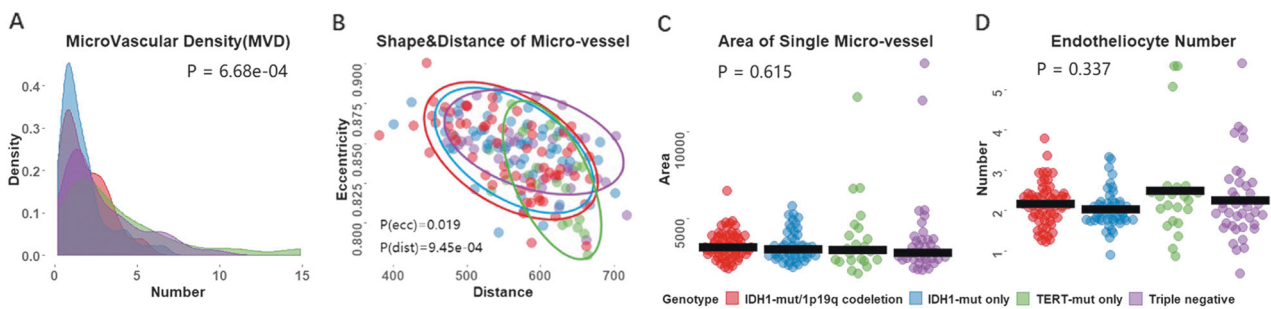
Fig. 8 Comparison of the vascularity in lower grade tumors. **a** The probability distribution map of microvascular density. **b** The scatter diagram of the average eccentricity and the average distance from cluster center of microvessels (the principal components of each subgroup are circled by an ellipse of the corresponding color). **c** The jitter graph of the average area of microvessel (the mean value is given by the black line). **d** The jitter graph of the average number of endothelial cell per microvessel (the mean value is given by the black line). *P* values obtained by significance analysis are given in the graph

Validation of prognosis

All cases with prognostic information were clustered into two groups by 500 days of survival because studies show that the median survival time of GBM is 15–17 months. According to the cut-off values, the cohort was regrouped into high-risk and low-risk group (cases with feature close to the long-term patients are classified as low risk and vice versa), with each feature determining a grouping situation. Survival analyses were conducted on these grouping situations and the results showed a significant difference between groups clustered by %MVA (hazard ratio [HR], 2.843, log-rank = 0.00087, cut-off = 0.7225) (Fig. 9). The other microvascularities (A, D, E, Sup, L) can also reflect the different survival risks between groups (Fig. S5).

Discussion

Angiogenesis relates to the degree of malignancy of a tumor. The microvascular spatial pattern could be regarded as a biomarker to predict patient prognosis. Currently, the quantitative analysis of angiogenesis is considered as a critical indicator to assess whether antiangiogenesis targeted therapy is effective or not.

The conventional approaches for qualitative or quantitative microvascular assessment are mainly based on chemical, biological, and manual methods. The most typical method of microvascular assessment consists of qualitative and quantitative measurement of vascular endothelial growth factor (VEGF) gene expression. Immunohistochemistry technology and RT-PCR are two popular approaches for analyzing gene expression. However, the immunohistochemical result has strong subjectivity and is therefore not accurate. PCR has high accuracy, but the operation is complex and the cost is high. Moreover, the qualitative and quantitative result of PCR is strongly affected by the test sample, and the accuracy is reduced when the sample is not pure. Thus, machine-learning-based image processing of H&E specimens will be a more objective and accurate method for the qualitative and quantitative assessment of angiogenesis.

As the degree of malignancy increases, the density of microvessels rises, which is supported by a considerable
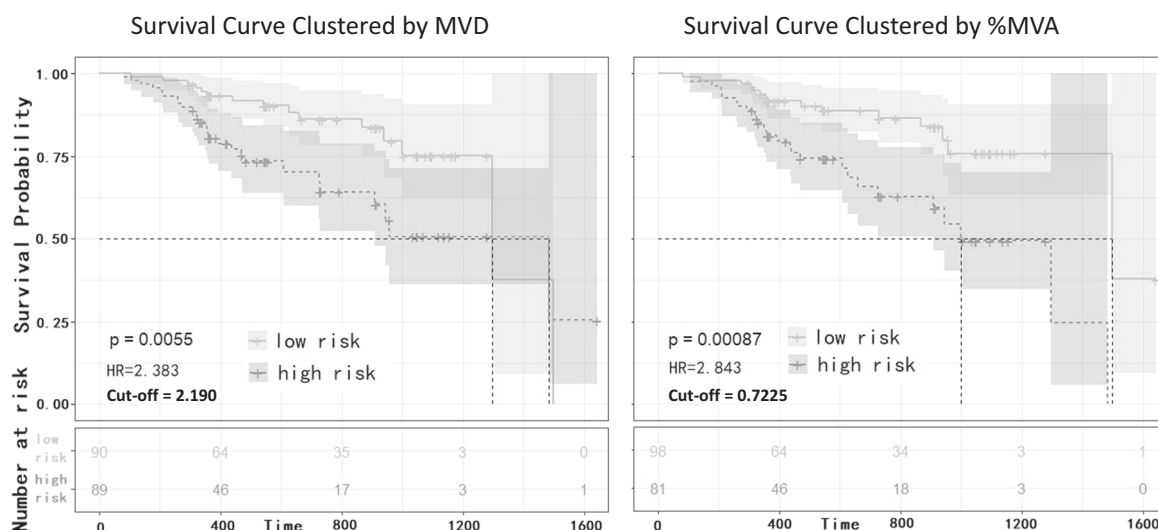
Fig. 9 Kaplan–Meier plots show the OS for patients with prognostic information, stratified to low- or high-risk group according to results of MVD clustering (left) and %MVA clustering (right). The hazard ratio, the original cut-off value, and significance are given in the graph

amount of molecular biology research. Variation analysis shows that microvessels in GBM are superior in terms of both quantity and area than those in astrocytoma and oligodendroglioma, which is in accordance with the classification standard of GBM from the WHO 2016 guidelines. Our results are consistent with previous conclusions, and the results further confirm the effectiveness of the proposed method for assisting pathologists to make more accurate diagnoses.

Since 2016, the diagnosis of glioma has entered the molecular age. Molecular diagnosis is more accurate in the prediction of glioma malignancy and the assessment of prognosis. Hai Yan et al. grouped glioma into several molecular types via the status of IDH/TERT/1p19q. IDH-mut only tends to develop astrocytoma, TERT-mut only tends to become GBM and IDH-mut/1p/19q codeletion tends to be oligodendroglioma. We examined the microvascularity of the four molecular subtypes (i.e., IDH-mut only, TERT-mut only, IDH-mut/1p/19q codeletion and triple Negative). Microvascular hyperplasia is commonly discovered in higher grade gliomas and could be regarded as a pathological indicator for malignancy [22]. In the comparison of all glioma cases, the microvascularization of TERT-mut only was more significant than the others, followed by the triple negative. Statistically, our findings are supported by the clinical data that the majority of TERT-mut only are pathologically classified as GBM [27, 28]. The diagnostic criteria for GBM, particularly gliomas with higher grade and malignancy, are the proliferation of abnormal microvessels. On the other hand, cases of TERT-mutation only often develop into glioblastoma. So there is a potential biological relationship between GBM diagnosis and microvascular assessment. In addition, triple negative

consists of quite a few GBM cases. The large number of GBM cases contributes to microvascularization to a certain extent and partly explains the high degree of angiogenesis in these two subtypes. The molecular information indicates that the proposed method is feasible and accurate.

Antiangiogenic therapy, such as VEGF inhibitors (e.g., bevacizumab), is an important method of cancer treatment. However, this treatment is ineffective in many cases. According to the subtyping method of The Caner Genome Atlas (TCGA), gliomas can be classified as Mesenchymal, Proneural, Neural, and Classical type [29]. Clinical research indicates that VEGF inhibitors have a curative effect on mesenchymal gliomas but only in the short term, through prolonging progression-free survival but not overall survival [30]. Gliomas with TERT-mut only are common in the Mesenchymal type where the differentiation degree of tumor cells is low and the malignancy of the tumor is high. As the microvascularization of TERT-mut only shows in our study, in the comparison between lower grade gliomas (i.e., astrocytoma and oligodendroglioma), TERT-mut only and triple negative types show a high level of microvascular quantity and area, an equal degree of proliferation and an even slightly smaller area of single vessels. Microcosmic variation exists only in the quantity of cells instead of the cellular morphology, which causes the growth of the neo-vessels, formation of the vessel networks, and the unchanged size of single vessels. This phenomenon could explain why molecular targeted therapy is effectively toxic to a number of tumor cells in the early stage, but the effect is not obvious with drug resistance in the late stage. Therefore, our proposed method could provide information on whether the patient can be given antiangiogenic treatment.

As a measure of recovery and prognosis, the OS directly indicates the malignancy of the glioma. Cases with a high degree of angiogenesis tend to have a high risk of death and a short period of survival, which was confirmed by histology and molecular typing. Our microvascular analysis also supports this point. The microvascular features extracted by our model are effectively able to distinguish high- or low-risk patients. Therefore, our method can distinguish patients with a high-risk of death due to a high degree of angiogenesis who may be benefited from antiangiogenic treatment. Thus, the proposed model has considerable potential for clinical application.

The potential advantage of our method is to help pathologists to make histological diagnosis more accurate, reduce subjective bias, and make diagnosis faster. In addition, it can assist physicians to make a more accurate judgment of prognosis, so as to guide whether to adopt more aggressive chemoradiotherapy or targeted treatment.

Although the proposed model can qualitatively and quantitatively assess the microvascularity in histological specimens of gliomas, limitations do exist in our study. (1) The property of microvascular pattern is shown to be a prognostic indicator, but we did not conduct more comprehensive analysis. By combining other prognostic signatures with statistical significance in multivariate analysis, gliomas can be further classified into groups with more distinct survival times, which will be more meaningful. (2) The accuracy of microvessel recognition has a big margin of improvement due to the segmentation error and the over counting, especially in larger pathological images with complex content. The microvascular assessment results can also be biased by the unrelated tissue specimen such as large areas of normal cortex or dissociative vessels. Both the accurate location of the region of interest and the improvement of recognition algorithm are the focus of our study in the next step. (3) Treatment based on the grading of microangiogenesis is a potential therapeutic strategy for glioma, but has not been studied due to the small number of antiangiogenesis treatment cases. We will collect more information from patients who receive antiangiogenesis treatment and validate the feasibility of our method via targeted research in the future.

Compliance with ethical standards

Conflict of interest The authors declare that they have no conflict of interest.

Publisher's note: Springer Nature remains neutral with regard to jurisdictional claims in published maps and institutional affiliations.

References

1. Ostrom QT, Gittleman H, Liao P, Rouse C, Chen Y, Dowling J, et al. CBTRUS statistical report: primary brain and central nervous system tumors diagnosed in the United States in 2007–2011. Neuro Oncol. 2014;16:iv1–iv63.
2. Louis DN, Perry A, Reigenberger G, Von Deimling A, Figarella-Branger D, Cavenee WK, et al. The 2016 WHO classification of tumours of the central nervous system: a summary. Acta Neuropathol. 2016;131:803–20.
3. Jasen M, Yip S, Louis DN. Molecular pathology in adult gliomas: diagnostic, prognostic, and predictive markers. Lancet Neurol. 2010;9:717–26.
4. Eckel-Passow JE, Lanchance DH, Molinaro AM, Walsh KM, Decker PA, Sicotte H, et al. Glioma groups based on 1p/19q, IDH, and TERT promoter mutations in tumors. N Engl J Med. 2015;372:2499–508.
5. Killela PJ, Pirozzi CJ, Healy P, Reitman ZJ, Lipp E, Rasheed BA, et al. Mutations in IDH1, IDH2, and in the TERT promoter define clinically distinct subgroups of adult malignant gliomas. Oncotarget. 2014;5:1515–25.
6. Brem S, Cotran R, Folkman J. Tumor angiogenesis: a quantitative method for histologic grading. J Natl Cancer Inst. 1972;48:347.
7. Folkerth RD. Descriptive analysis and quantification of angiogenesis in human brain tumors. J Neuro-Oncol. 2000;50:165–72.
8. Leon SP, Folkerth RD, Black PM. Microvessel density is a prognostic indicator for patients with astroglial brain tumors. Cancer. 1996;77:362–72.
9. Wesseling P, van der Laak JA, Link M, Teepen HL, Ruiter DJ. Quantitative analysis of microvascular changes in diffuse astrocytic neoplasms with increasing grade of malignancy. Hum Pathol. 1998;29:352–8.
10. Van den Bent MJ. Interobserver variation of the histopathological diagnosis in clinical trials on glioma: a clinician's perspective. Acta Neuropathol. 2010;120:297–304.
11. Gurcan MN, Boucheron LE, Can A, Madabhushi A, Yener B. Histopathological image analysis: a review. IEEE Rev Biomed Eng. 2009;2:147–71.
12. Kong J, Cooper L, Wang F, Gao J, Teodoro G, Scarpace L, et al. Machine-based morphologic analysis of glioblastoma using whole-slide pathology images uncovers clinically relevant molecular correlates. PLoS ONE. 2013;8:e81049.
13. Ghaznavi F, Evans A, Madabhushi A, Feldman M. Digital imaging in pathology: whole-slide imaging and beyond. Annu Rev Pathol-Mech Dis. 2013;8:331–59.
14. Xing F, Xie Y, Yang L. An automatic learning-based framework for robust nucleus segmentation. IEEE Trans Med Imaging. 2016;35:550–66.
15. Sirinukunwattana K, Ahmed Raza SE, Tsang Yee-Wah, Snead DR, Cree IA, Rajpoot NM. Locality sensitive deep learning for detection and classification of nuclei in routine colon cancer histology images. IEEE Trans Med Imaging. 2016;35:1196–206.
16. Ertosun MG, Rubin DL. Automated grading of gliomas using deep learning in digital pathology images: a modular approach with ensemble of convolutional neural networks. AMIA Annu. Symp. Proc. 2015;2015:1899–908.
17. Cireşan DC, Giusti A, Gambardella LM, Schidhuber J. Mitosis detection in breast cancer histology images with deep neural networks. Med Image Comput Comput Assist Interv. 2013;16:411–8.

18. Liu Y, Gadepalli K, Norouzi M, Dahl GE. Detecting cancer metastases on gigapixel pathology images. https://arxiv.org/abs/1703.02442.

19. Ronneberger O, Fischer P, and Brox T U-Net: convolutional networks for biomedical image segmentation. Med Image Comput Comput Assist Interv. 2015:2015:234–41.

20. Di Ieva A, Bruner E, Widhalm G, Minchev G, Tschabitscher M, Grizzi F. Computer-assisted and fractal-based morphometric assessment of microvascularity in histological specimens of gliomas. Sci Rep. 2012;2:429.

21. Chen L, Lin ZX, Lin GS, Zhou CF, Chen YP, Wang XF, et al. Classification of microvascular patterns via cluster analysis reveals their prognostic significance in glioblastoma. Hum Pathol. 2015;46:120–8.

22. Sun H, Guo D, Su Y, Yu D, Wang Q, Wang T, et al. Hyperplasia of pericytes is one of the main characteristics of microvascular architecture in malignant glioma. PLoS ONE. 2014;9: e114246.

23. Long J, Shelhamer E, Darrell T. Fully convolutional networks for semantic segmentation. IEEE CVPR. 2015;79:3431–40.

24. Szegedy C, Liu W, Jia Y, Sermanet P. Going deeper with convolutions. IEEE CVPR. 2015:1–9.

25. Simonyan K, Zisserman A. Very deep convolutional networks for large-scale image recognition. Computer Science. 2014. http://cn.arxiv.org/abs/1409.1556.

26. Birner P, Piribauer M, Fischer I, Gatterbauer B, Marosi C, Ambros PF, et al. Vascular patterns in glioblastoma influence clinical outcome and associate with variable expression of angiogenic proteins: evidence for distinct angiogenic subtypes. Brain Pathol. 2003;13:133–43.

27. Koelsche C, Sahm F, Capper D, Reuss D, Sturm D, Jones DT, et al. Distribution of TERT promoter mutations in pediatric and adult tumors of the nervous system. Acta Neuropathol. 2013;126:907–15.

28. Liu X, Wu G, Shan Y, Hartmann C, von Deimling A, Xing M. Highly prevalent TERT promoter mutations in bladder cancer and glioblastoma. Cell Cycle. 2013;12:1637–8.

29. Verhaak RG, Hoadley KA, Purdom E, Wang V, Qi Y, Wilkerson MD, et al. Integrated genomic analysis identifies clinically relevant subtypes of glioblastoma characterized by abnormalities in PDGFRA, IDH, EGFR, and NF1. Cancer Cell. 2010;17:98–110.

30. Winterhoff BJ, Kommoss S, Oberg AL. Bevacizumab and improvement of progression-free survival (PFS) for patients with the mesenchymal molecular subtype of ovarian cancer. J Clin Oncol. 2014;32:5509.